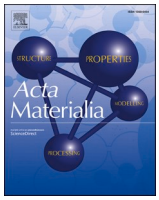
Acta Materialia 307 (2026) 121981



Contents lists available at ScienceDirect

Acta Materialia

journal homepage: www.elsevier.com/locate/actamat



Three-dimensional crystallographic and local variant configuration analysis of lath martensite in medium-carbon steel

Akinobu Shibata [a,*], Goro Miyamoto [b], Shigekazu Morito [c], Akiko Nakamura [d], Taku Moronaga [d], Houichi Kitano [a], Ivan Gutierrez-Urrutia [a], Toru Hara [a]

[a] Research Center for Structural Materials, National Institute for Materials Science (NIMS), 1-2-1, Sengen, Tsukuba 305-0047, Japan
[b] Institute for Materials Research, Tohoku University, 2-1-1, Katahira, Aoba-ku, Sendai 980-8577, Japan
[c] Department of Physics and Materials Science, Shimane University, 1060, Nishikawatsu, Matsue, Shimane 690-8504, Japan
[d] Research Network and Facility Services Division, National Institute for Materials Science (NIMS), 1-2-1, Sengen, Tsukuba 305-0047, Japan

ARTICLE INFO

Keywords:
Martensitic transformation
Steel
Transmission electron microscopy
Serial-sectioning
Crystallography
Variant configuration

ABSTRACT

The microstructures and crystallographic features of lath martensite in a medium-carbon steel were investigated using focused ion beam-scanning electron microscopy serial sectioning and automated crystallographic orientation mapping in transmission electron microscopy techniques. The analysis revealed that, despite the complex and interwoven overall morphology, individual laths possess well-defined, plate-like shapes. Habit plane / lath boundary plane orientations determined by two-surface trace analysis spanned a range from $(2\ 5\ 2)_A$ to $(2\ 9\ 5)_A$ in the austenite coordinate system and were centered around $(3\ 8\ 1)_M$ in the martensite coordinate system. These results are consistent with predictions from the phenomenological theory of martensitic crystallography incorporating double lattice-invariant deformations and a high degree of tetragonality. Crystallographic variant analysis showed pairing tendencies among variants sharing parallel close-packed planes, along with the presence of nanoscale twin-related domains distinct from typical $(1\ 1\ 2)_M$ transformation twins. These domains were interpreted as twin-orientation-related intralath structures that formed ahead of the longitudinal growth front of a martensite plate and were subsequently embedded by its lateral growth. Micromechanics calculations further suggested that stress-induced variant selection, enhanced by high tetragonality, plays a critical role in the preferential formation of these twin-orientation-related intralath structures. Although the lath has traditionally been regarded as the smallest structural unit, detailed characterization of a twin-orientation-related intralath structure reveals an additional level of hierarchy, distinct from conventional defect substructures, fundamentally redefining the established microstructural concept of lath martensite.

1. Introduction

Growing demands for advanced high-strength steels, aimed at improving the performance and efficiency of transportation and energy systems, have led to renewed interest in martensitic steels as key structural metallic materials. Although martensite is a well-known microstructure in steels [1], the fundamental mechanisms that govern its formation and evolution of microstructure are still not fully understood. This lack of comprehensive understanding poses significant obstacles to designing and developing next-generation high-strength steels with optimized mechanical performance.

The microstructure of lath martensite exhibits a hierarchical structure defined by morphological features, comprising laths, blocks, packets, and prior austenite grains [2–7]. According to the traditional definition, a lath is the smallest structural single-crystal unit, characterized by a high dislocation density and, particularly in steels containing more than approximately 0.2 % carbon, by the presence of transformation twins [7–9]. A block consists of laths with nearly identical crystallographic orientations, while a packet contains several blocks sharing similar habit plane orientations and close-packed planes. A prior austenite grain corresponds to the grain in the parent austenite phase before the martensitic transformation. These hierarchical microstructures result in anisotropic plastic deformation as well as branching and meandering brittle crack propagation [10–14].

As the origin of the complex lath martensite structure, crystallographic analysis on variant pairings has been extensively conducted in

* Corresponding author.
E-mail address: SHIBATA.Akinobu@nims.go.jp (A. Shibata).

https://doi.org/10.1016/j.actamat.2026.121981
Received 27 October 2025; Received in revised form 14 January 2026; Accepted 1 February 2026
Available online 3 February 2026
1359-6454/© 2026 The Author(s). Published by Elsevier Inc. on behalf of Acta Materialia Inc. This is an open access article under the CC BY license (http://creativecommons.org/licenses/by/4.0/).

recent years, and the key findings are summarized below. Using electron backscatter diffraction in a scanning electron microscope (SEM-EBSD) and transmission electron microscopy (TEM), Morito et al. [4,5] performed a detailed crystallographic analysis of as-quenched lath martensite. The analysis assumed the Kurdjumov-Sachs (K-S) orientation relationship between martensite and its parent austenite, specifically $(1\ 1\ 1)_A$ // $(0\ 1\ 1)_M$ and $[-1\ 0\ 1]_A$ // $[-1\ -1\ 1]_M$ (the subscripts "A" and "M" indicate the coordinate systems of austenite and martensite, respectively). Hereafter, the K-S variant notation shown in Table 1 [15] will be adopted to describe the variant pairings. Their study demonstrated that each packet consisted of three blocks in low-carbon steels (0.0026 - 0.38 mass % C). Each block was further subdivided into laths associated with two specific K-S variants (V1/V4, V2/V5, and V3/V6), referred to as sub-blocks, exhibiting small misorientations of approximately 10°. Conversely, high-carbon steel (0.61 mass % C) displayed a different arrangement, where each packet contained six possible blocks, each consisting of a single K-S variant (V1 - V6). Stormvinter et al. systematically studied variant pairings of martensite in as-quenched Fe-C alloys, specifically focusing on effect of carbon content using SEM-EBSD [16]. At low carbon contents, variant pairings sharing a common habit plane predominantly occur. With increasing carbon content, the frequency of sub-block pairings, such as V1/V4, tends to decrease, while the fraction of twin-related variant pairings, such as V1/V2, increases. At high carbon contents, variant pairings involving V1, V6, V16 and V17, which are favorable for the self-accommodation of transformation strain [17–21], become dominant. Kumar et al. precisely evaluated the residual stress in the parent austenite phase and proposed a correlation between the residual stress and variant selection in as-quenched lath martensite [22]. Furthermore, external factors such as applied deformation, deformation microstructures in austenite, austenite grain size, among others, have been thoroughly investigated [23–30].

In addition to variant pairings, habit plane (lath boundary plane) orientations and inter-variant boundary plane orientations are important crystallographic parameters for discussing the underlying mechanism of microstructure evolution accompanying martensitic transformation. Although the phenomenological theory of martensite crystallography (PTMC) can predict various crystallographic features of martensite, such as habit plane orientation, shape deformation direction, among others [31–34], detailed experimental investigations of habit plane and inter-variant boundary plane orientations remain scarce. Marder and Krauss [2] used annealing twin boundaries as a reference for the orientation of the parent austenite phase and measured the habit plane orientation of lath martensite using optical microscopy images taken from different sections. Their results indicate that the habit plane orientation is approximately $\{5\ 7\ 5\}_A$, a finding that has been widely recognized to date. Sandvik and Wayman [35–37] examined the substructures and crystallographic characteristics of lath martensite formed under isothermal conditions using TEM. They found that the habit planes exhibited irrational orientations, approximately $\{5\ 7\ 5\}_A$ and $\{1\ 5\ 4\}_M$. Based on the three-dimensional (3D) morphology of lath martensite obtained by serial sectioning, Rowenhorst et al. [38] reported that the boundary planes of coarse martensite crystals were $\{0.113\ 0.946\ 0.304\}_M$ and $\{0.288\ 0.947\ 0.142\}_M$. Similarly, Morito et al. [39] found that the boundaries between martensite variants were $\{0.615\ 0.578\ 0.537\}_A$ and $\{0.632\ 0.586\ 0.500\}_A$. Recently, Mosayebi et al. [40–42] performed a 3D characterization of the lath martensite structure using large-volume 3D EBSD. Their results indicate that the habit plane orientation is close to $\{5\ 7\ 5\}_A$ with a slight shift toward $\{1\ 2\ 1\}_A$, and that the orientations of the inter-variant boundary planes correspond to $\{0\ 1\ 1\}_M$, exhibiting symmetric tilt, twist, or mixed character. Beladi et al. [43] statistically investigated the habit plane and inter-variant boundary characteristics in the lath martensite structure through precise orientation analysis based on SEM-EBSD. Their results explored that specific inter-variant boundaries frequently align with $\{0\ 1\ 1\}_M$ planes, often exhibiting $\{0\ 1\ 1\}_M$-type symmetric tilt and twist characters. In addition to the previous studies, systematic studies on the orientations of habit plane / lath boundary plane in lath martensite structures are necessary to deepen our understanding of the underlying mechanism of martensitic transformation.

It should be noted that most of the reported crystallographic features [2,38–43], excluding those for isothermally transformed martensite [35], concern aggregated lath structures rather than individual laths. Investigating the crystallography of individual laths enhances our understanding of martensitic transformation, given that the crystallographic characteristics of an individual lath, as the most elementary structural unit, are closely linked to the initial transformation process. Recently, we have developed 3D microstructure analysis techniques that combine focused ion beam-scanning electron microscopy (FIB-SEM) serial sectioning and TEM, including automated crystallographic orientation mapping (ACOM-TEM), and studied the substructures and crystallographic features of individual laths in interstitial-free (IF) steel

Table 1
Twenty-four crystallographic martensite variants in the K-S relationship [15].

Variant No.	Close-packed plane parallel relation		Close-packed direction parallel relation	Bain	Misorientation from V1 (deg)
1	CP1	$(1\ 1\ 1)_A$ // $(0\ 1\ 1)_M$	$[-1\ 0\ 1]_A$ // $[-1\ -1\ 1]_M$	B1	-
2		$(-1\ -1\ -1)_A$ // $(0\ 1\ 1)_M$		B2	60.0
3		$(1\ 1\ 1)_A$ // $(0\ 1\ 1)_M$	$[0\ 1\ -1]_A$ // $[-1\ -1\ 1]_M$	B3	60.0
4		$(-1\ -1\ -1)_A$ // $(0\ 1\ 1)_M$		B1	10.5
5		$(1\ 1\ 1)_A$// $(0\ 1\ 1)_M$	$[1\ -1\ 0]_A$ // $[-1\ -1\ 1]_M$	B2	60.0
6		$(-1\ -1\ -1)_A$ // $(0\ 1\ 1)_M$		B3	49.5
7	CP2	$(1\ -1\ 1)_A$ // $(0\ 1\ 1)_M$	$[1\ 0\ -1]_A$ // $[-1\ -1\ 1]_M$	B2	49.5
8		$(-1\ 1\ -1)_A$ // $(0\ 1\ 1)_M$		B1	10.5
9		$(1\ -1\ 1)_A$ // $(0\ 1\ 1)_M$	$[-1\ -1\ 0]_A$ // $[-1\ -1\ 1]_M$	B3	50.5
10		$(-1\ 1\ -1)_A$ // $(0\ 1\ 1)_M$		B2	50.5
11		$(1\ -1\ 1)_A$ // $(0\ 1\ 1)_M$	$[0\ 1\ 1]_A$ // $[-1\ -1\ 1]_M$	B1	14.9
12		$(-1\ 1\ -1)_A$ // $(0\ 1\ 1)_M$		B3	57.2
13	CP3	$(-1\ 1\ 1)_A$ // $(0\ 1\ 1)_M$	$[0\ -1\ 1]_A$ // $[-1\ -1\ 1]_M$	B1	14.9
14		$(1\ -1\ -1)_A$ // $(0\ 1\ 1)_M$		B3	50.5
15		$(-1\ 1\ 1)_A$ // $(0\ 1\ 1)_M$	$[-1\ 0\ -1]_A$ // $[-1\ -1\ 1]_M$	B2	57.2
16		$(1\ -1\ -1)_A$ // $(0\ 1\ 1)_M$		B1	20.6
17		$(-1\ 1\ 1)_A$ // $(0\ 1\ 1)_M$	$[1\ 1\ 0]_A$ // $[-1\ -1\ 1]_M$	B3	51.7
18		$(1\ -1\ -1)_A$ // $(0\ 1\ 1)_M$		B2	47.1
19	CP4	$(1\ 1\ -1)_A$ // $(0\ 1\ 1)_M$	$[-1\ 1\ 0]_A$ // $[-1\ -1\ 1]_M$	B3	50.5
20		$(-1\ -1\ 1)_A$ // $(0\ 1\ 1)_M$		B2	57.2
21		$(1\ 1\ -1)_A$ // $(0\ 1\ 1)_M$	$[0\ -1\ -1]_A$ // $[-1\ -1\ 1]_M$	B1	20.6
22		$(-1\ -1\ 1)_A$ // $(0\ 1\ 1)_M$		B3	47.1
23		$(1\ 1\ -1)_A$ // $(0\ 1\ 1)_M$	$[1\ 0\ 1]_A$ // $[-1\ -1\ 1]_M$	B2	57.2
24		$(-1\ -1\ 1)_A$ // $(0\ 1\ 1)_M$		B1	21.1

and low-carbon (0.2C) steel [7]. The results indicated that the morphology of the so-called lath exhibited a wedge-shaped plate instead of the ideal lath shape. The habit plane orientations identified by two-surface trace analysis using 3D morphology of laths were distributed from $(5\,7\,5)_A$ to $(1\,1\,1)_A$ in the IF steel, whereas they were near to $(1\,2\,1)_A$ and that predicted based on the PTMC in the 0.2C steel.

Medium-carbon martensitic steels have attracted increasing attention in recent years due to high demands of structural components subjected to high mechanical loads. Advances in microstructure control techniques for the medium-carbon martensitic steels can further expand their applicability in automotive, aerospace, and energy industries. Compared with low-carbon steels, the microstructures of medium-carbon martensitic steels are significantly more complex [4,16], resulting in an insufficient understanding of their formation mechanisms and the origins of their crystallographic features. In the present study, the microstructure and crystallographic features of lath martensite in medium-carbon steel were investigated via FIB-SEM serial sectioning and advanced TEM. The mechanisms underlying the development of these characteristics are also discussed in relation to our previous studies on lath martensite in IF and 0.2C steels [7].

2. Experimental procedure

The material used in the present study was manganese-added medium-carbon steel (2Mn-0.5C steel). The chemical composition (in mass %) of the material was C: 0.493, Si: 0.01, Mn: 2.04, P: <0.002, S: 0.0008, Fe: balance. The hot-rolled plate was austenitized at 1000 °C for 600 s, followed by water quenching. According to the reported equation [44],

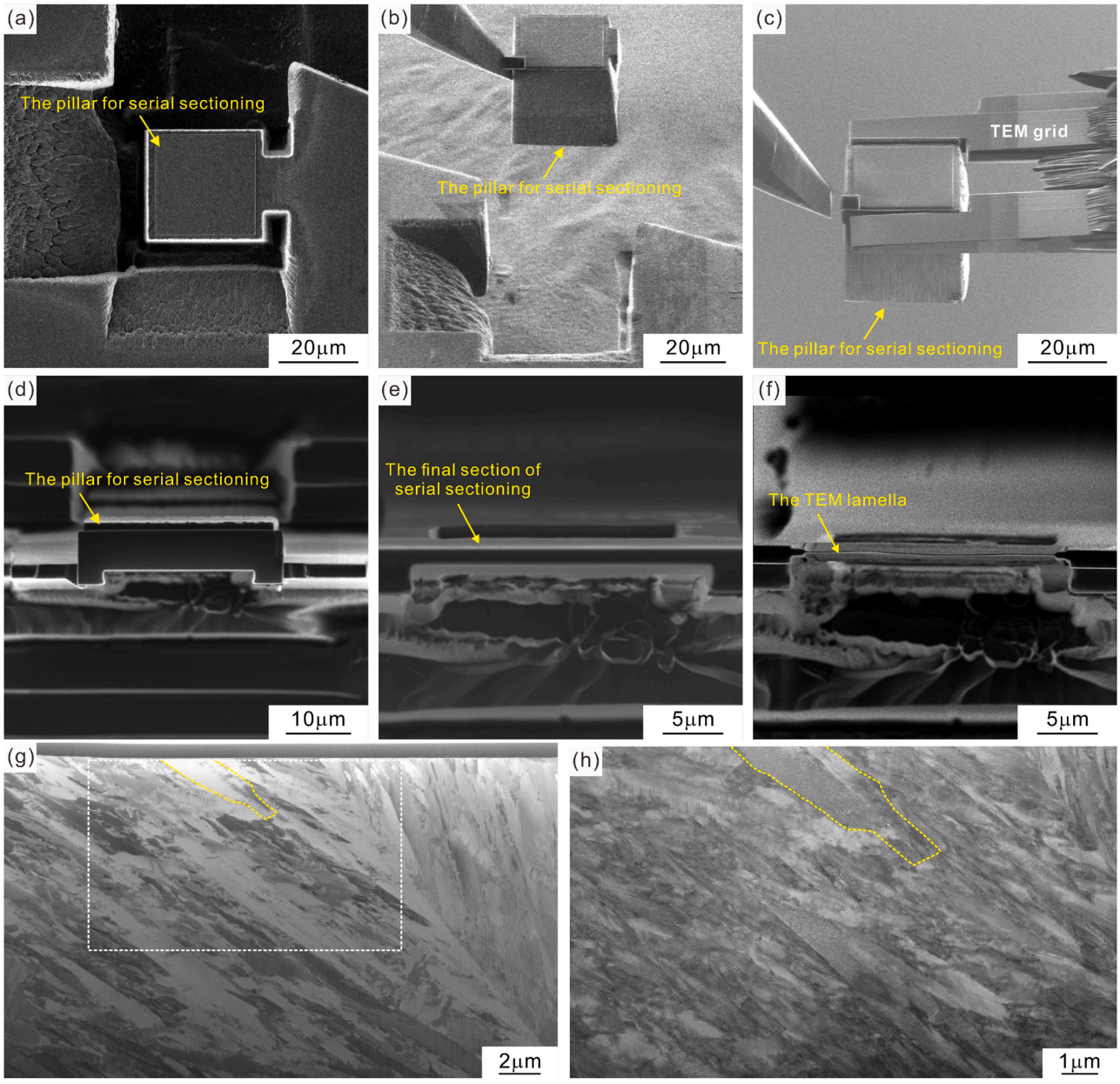


Fig. 1. The detailed procedure used to prepare the specimen for FIB-SEM serial sectioning and TEM/STEM observation: (a-c) SEM images showing (a) the specimen after FIB machining, (b, c) after the specimen was lifted out and mounted onto a TEM grid, which was reshaped to fit the specimen. (d-f) Scanning ion microscopy images showing the specimen (d) before FIB-SEM serial sectioning, (e) after FIB-SEM serial sectioning, and (f) for TEM/STEM observation after FIB milling. (g, h) Identical area observation results of (g) the SEM image of the final section of FIB-SEM serial sectioning and (h) the STEM image corresponding to the white rectangle in (g) (the same microstructural unit is indicated by yellow broken lines).

the estimated martensitic transformation start (Ms) temperature is equal to 264 °C.

The microstructure of the heat-treated specimen was observed by optical microscopy and SEM-EBSD (Zeiss: Sigma and Bruker: QUANTAX-EBSD system) with an acceleration voltage of 20 kV. The procedure for fabricating the specimen for FIB-SEM serial sectioning and TEM analysis is illustrated in Fig. 1. A pillar with dimensions of approximately 20 μm × 20 μm × 30 μm was lifted out from the heat-treated bulk sample and mounted onto a TEM grid as shown in Fig. 1 (a – c) using FIB (ThermoFisher Scientific: Scios 2). The pillar was shaped into approximately 20 μm × 20 μm × 6 μm (Fig. 1(d)) and subjected to FIB-SEM serial sectioning (Hitachi High-Tech: SMF-1000) [45]. The specimen was serially milled at 5 nm intervals using a Ga ion beam operated at an accelerating voltage of 30 kV and a beam current of 0.65 nA. Each cross-sectional microstructure was imaged with an in-lens electron detector under a low accelerating voltage of 0.5 kV. The resulting image stack was processed using the ORS Dragonfly software to perform positional registration of the serial sectioning images and to reconstruct the 3D morphology of lath martensite. Some of the structural units in the lath martensite structure were extracted from each serially acquired SEM image using a customized image-processing workflow. The SEM images were first denoised and contrast-enhanced using the procedures described in [46]. Candidate regions were then identified using Otsu thresholding. Connected-component labeling, distance transformation, and watershed segmentation were applied to merge fragmented domains and to delineate adjacent features. The final regions were selected based on spatial continuity and morphological consistency. Since the pillar had already been mounted onto the TEM grid from the beginning (Fig. 1 (a – c)), a TEM thin foil was fabricated around the final section of serial sectioning using the FIB-SEM system (Fig. 1 (e, f)). The SEM image of the last section of FIB-SEM serial sectioning and the scanning transmission electron microscopy (STEM) image (Fig. 1 (g, h)) demonstrate that the alignment difference between the FIB-SEM and TEM analyses was negligibly small, as the same microstructural unit is indicated by yellow broken lines.

The substructures were examined by TEM and STEM (JEOL: JEM-2800, JEM-ARM300F) operated at accelerating voltages of 200 kV and 300 kV. The local crystal orientations were analyzed via ACOM-TEM (NanoMEGAS: ASTAR) using a step size of 5 nm. In ACOM-TEM, the recorded patterns were compared with a database of template patterns prepared with an orientation step of 1°, and the orientation of each point in the analyzed area was determined through this so-called pattern matching procedure. In addition, interpolation between template patterns with a 1° orientation difference was performed at a finer step of 0.1°. Because the misorientation profiles actually obtained by ACOM-TEM often exhibited oscillations with an amplitude of approximately 1° [7], the practical orientation resolution of ACOM-TEM is estimated to be in the range of 0.1 to 1°. For the crystallographic analysis, the K-S variant notation summarized in Table 1 [15] was used. Table 1 [15] also provides the Bain correspondence, where the compression axes in Bain deformation of B1, B2, and B3 are $[0\ 0\ 1]_A$, $[1\ 0\ 0]_A$, and $[0\ 1\ 0]_A$, respectively, along with the misorientations from V1. The variant determination was performed by comparing the experimentally obtained $<0\ 0\ 1>_M$ pole figure with the ideal $<0\ 0\ 1>_M$ poles of the twenty-four K-S variants.

3. Results

3.1. Morphology and habit plane orientation of the lath

Fig. 2 (a, b) shows an optical microscopy image and the corresponding EBSD orientation map of the heat-treated specimen. In the EBSD orientation map of Fig. 2(b), the color coding represents the crystal orientation parallel to the normal direction of the observed section, as indicated by the inserted stereographic triangle at the upper right corner. The observed microstructure exhibits a typical lath martensite structure, characterized by the hierarchical arrangement of blocks and packets within a prior austenite grain, with an average prior austenite grain size of 122 μm. No obvious plate-shaped martensite (e.g., lenticular or thin plate martensite) was observed. Fig. 3 (a, b) depicts the 3D morphology of the lath martensite reconstructed from a series of SEM images of each section acquired by FIB-SEM serial sectioning. The voxel size of the 3D reconstructed images is 6.25 nm × 6.25 nm × 5 nm. Fig. 1 (g, h), as well as our previous study [7], indicates that channeling contrast images acquired with the SEM/in-lens detector can clearly reveal individual lath morphologies and the locations of lath boundaries. Therefore, the 3D reconstructed images presented in Fig. 3 (a, b) enable detailed investigation of the lath morphology and the

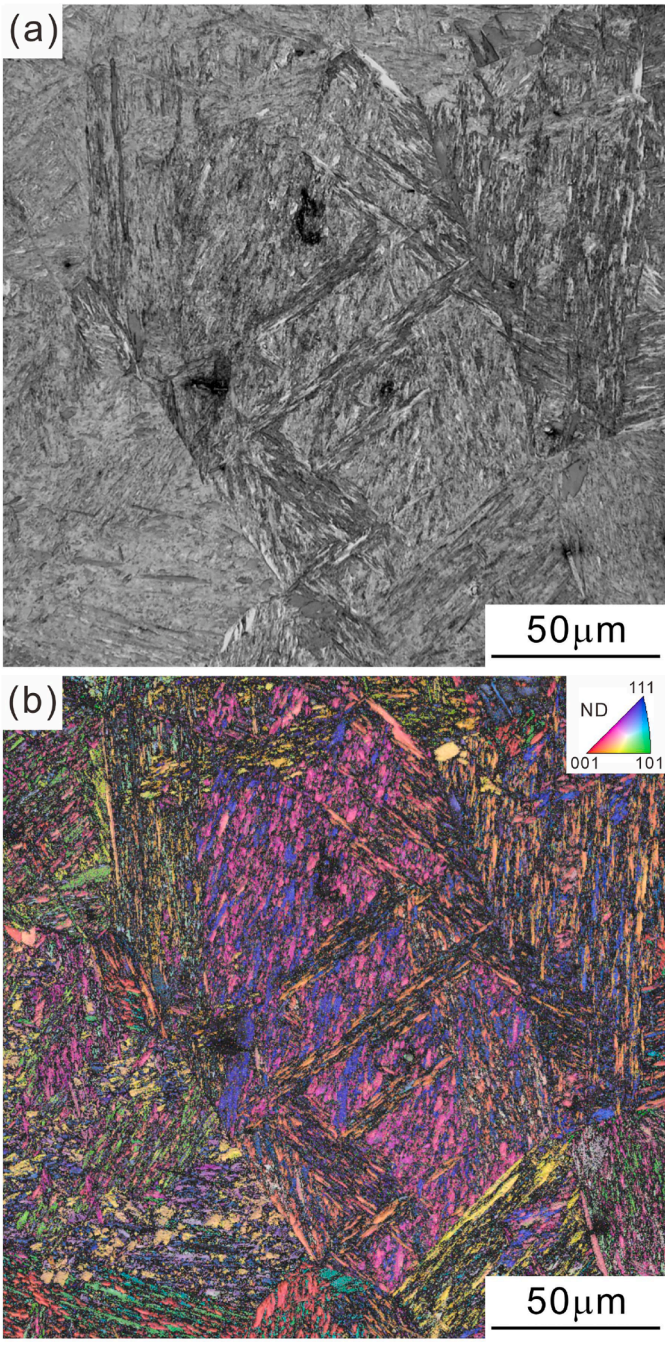


Fig. 2. (a) Optical microscopy image and (b) corresponding EBSD orientation map of the heat-treated specimen. The colors in the EBSD orientation map represent the crystal orientation parallel to the normal direction according to the inserted stereographic triangle.

crystallography of the lath boundaries. Representative boundaries of the laths identified from the reconstructed volume are delineated with red broken lines in the figure. While the overall morphology of lath structure appears complex and interwoven, each individual lath exhibits a relatively well-defined, plate-like shape, rather than a literal "lath"-like morphology as implied by the terminology. Such a plate-like morphology, which is characteristic of individual laths, has also been confirmed in other martensitic steels, including IF steel and 0.2C steel in our previous work [7]. This suggests that the observed morphological feature is intrinsic to the nature of lath martensite structure across a range of alloy compositions.

The crystallographic orientations of lath boundary planes, which correspond to habit planes of the lath, were identified via two-surface trace analysis, based on 3D morphological data and orientation data of both the martensite and parent austenite phases. The orientations were indexed as the observed martensite corresponds to V1 ($(1\ 1\ 1)_A$ // $(0\ 1\ 1)_M$, $[-1\ 0\ 1]_A$ // $[-1\ -1\ 1]_M$). Since the final section of FIB-SEM serial sectioning closely coincided with the region observed in the STEM (Fig. 1 (g, h)), we could incorporate high spatial-resolution crystallographic orientation data obtained using ACOM-TEM into the two-surface trace analysis. In addition, the orientations of the parent austenite phase were recalculated from the ACOM-TEM orientation data using the reconstruction algorithm proposed by Miyamoto et al. [47]. The reconstruction was performed using a cropped-square size of 5 $\mu m \times$ 5 μm and a spacing of 1.25 μm between neighboring squares, assuming an orientation relationship of $\phi_1 = 2.096978$ rad, $\Phi = 0.153508$ rad, $\phi_2 = 3.414253$ rad [48], and considering only data points with a confidence index ≥ 0.2. This reconstruction process enables the determination of parent austenite orientation even though the austenite phase transformed into martensite completely. In the images of the arbitrary orthogonal sections (XY, YZ, and ZX) of the reconstructed 3D volume, we manually selected the lath boundaries that were clearly visible. The habit plane / lath boundary plane orientation was determined from the cross product of the two line-vectors that correspond to the traces of the

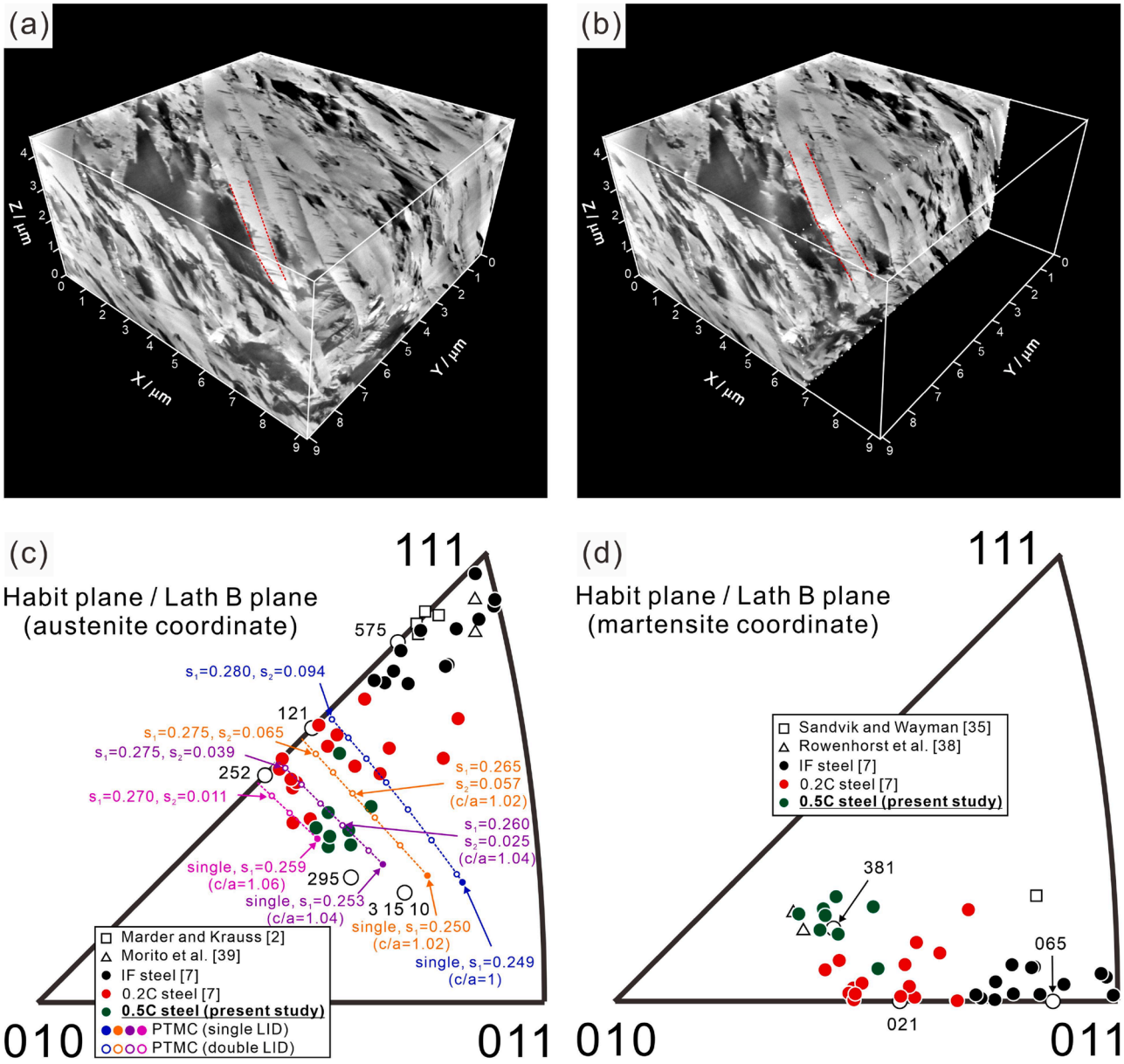


Fig. 3. (a, b) 3D reconstructed images of lath martensite via FIB-SEM serial sectioning and (c, d) stereographic triangles showing the orientations of habit planes / lath boundary planes (green circles) with respect to austenite coordinate system (c) and martensite coordinate system (d). The habit plane / lath boundary orientations reported in previous studies [2,7,35,38,39] and predicted based on the PTMC are plotted as well in (c, d).

same plane observed on two of the three sections. The plane orientations obtained from the three possible combinations of traces (XY – YZ, YZ – ZX, and ZX – XY) exhibited an orientation error that is equal to approximately 7°. Furuhara et al. [49] determined the orientation of grain boundary planes using two-surface trace analysis combined with EBSD data, and reported that the orientation of coherent annealing twin boundaries in an austenitic stainless steel, measured by two-surface trace analysis, deviated from the ideal $\{1\ 1\ 1\}_A$ plane by up to approximately 5°. The results of the two-surface trace analysis are presented in Fig. 3 (c, d), where the identified boundary plane orientations are plotted as green circles in the stereographic triangles with respect to both the austenite and martensite coordinate systems. The orientations of habit planes / lath boundary planes identified in the present study are distributed over a range between $(2\ 5\ 2)_A$ and $(2\ 9\ 5)_A$ in the austenite coordinate system, and are centered around $(3\ 8\ 1)_M$ in the martensite coordinate system. However, the orientations of habit planes / lath boundary planes show significant scatter. This dispersion of orientation could be attributed to the fact that the analyzed planes in the present study do not strictly correspond to the original habit planes of martensite, which are defined as the interphase boundary planes between martensite and austenite. Instead, the observed boundaries likely correspond to the boundary planes formed after the impingement of interphase boundaries between adjacent laths. We assume in the following that the measured orientations of the lath boundary planes reasonably approximate the original habit plane orientations at the interphase boundary between martensite and austenite. For comparison, previously reported orientations of habit planes / lath boundary planes [2,7,35,38,39] are also included in Fig. 3 (c, d). A clear dependence on carbon composition is evident, as the orientation of the habit plane / lath boundary plane progressively deviates from $(1\ 1\ 1)_A$ towards (2 5

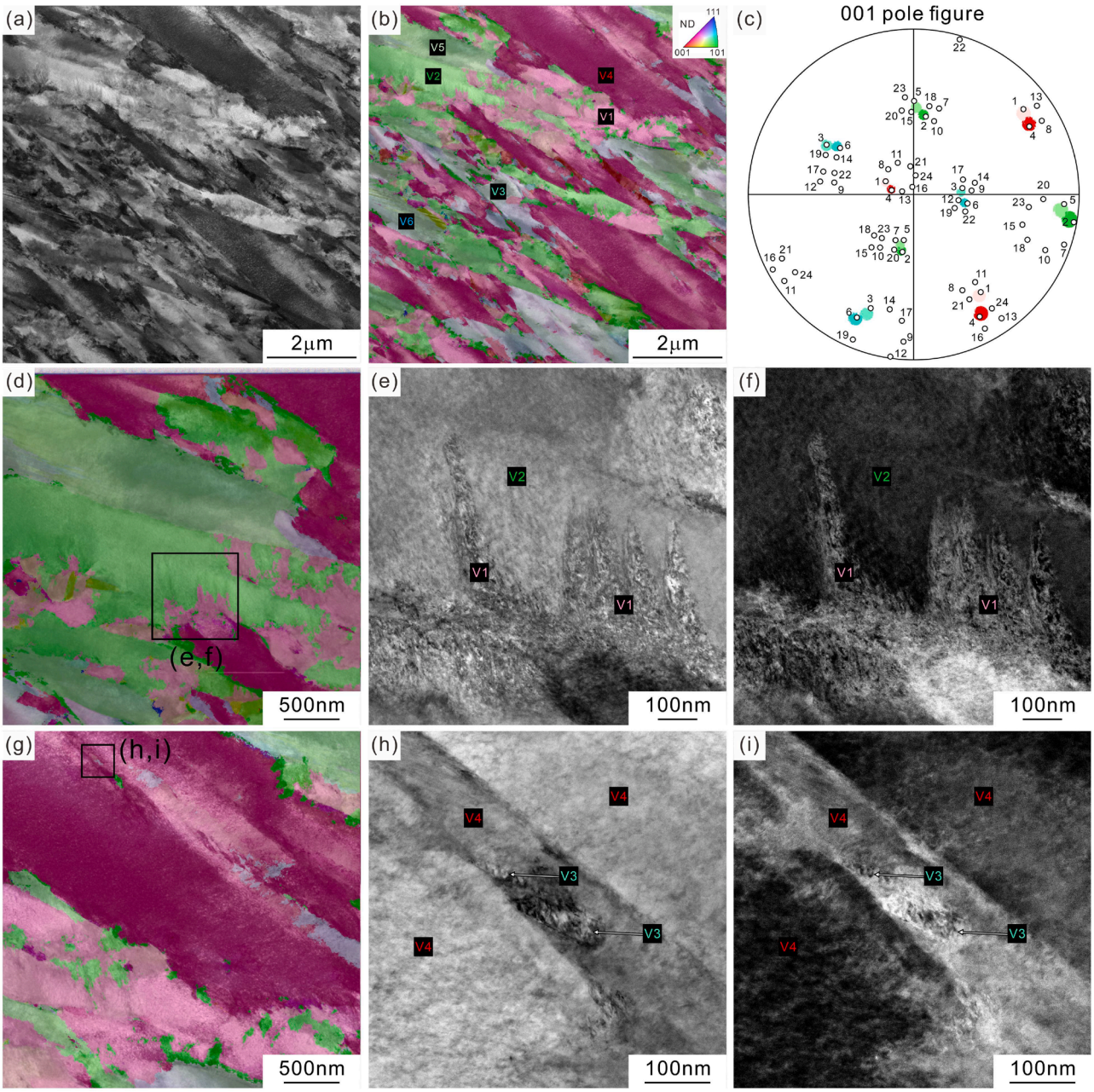


Fig. 4. (a, e, f, h, i) STEM images (a, e, h: bright-field STEM images, f, i: dark-field STEM images), (b, d, g) ACOM-TEM orientation maps, and (c) $<0\ 0\ 1>_M$ pole figure, in which the ideal poles of the twenty-four K-S variants, as well as those of the variants observed in (b), are plotted. The colors in the ACOM-TEM orientation maps represent the crystal orientation parallel to the normal direction according to the inserted stereographic triangle.

$2)_A$ or $(2\ 9\ 5)_A$ (from $(0\ 1\ 1)_M$ towards $(3\ 8\ 1)_M$) with increasing carbon content. The invariant plane orientations predicted based on the PTMC are also plotted in Fig. 3(c). The PTMC calculations incorporate the influence of martensite tetragonality as well as the magnitudes of the lattice-invariant deformation, which are essential parameters in determining the invariant plane orientations. The correlation between the experimentally identified habit plane / lath boundary plane orientations and the invariant plane orientations predicted from the PTMC calculations will be discussed in detail in a later section.

3.2. *Variant configurations*

Local variant configurations were analyzed using ACOM-TEM, and the results are presented in Fig. 4; (a, e, f, h, i) show STEM images (a, e, h: bright-field STEM images, f, i: dark-field STEM images), (b, d, g) display ACOM-TEM orientation maps, and (c) presents $<0\ 0\ 1>_M$ pole figure, in which the ideal poles of the twenty-four K-S variants, as well as those of the variants observed in (b), are plotted. The colors in the ACOM-TEM orientation maps represent the crystal orientation parallel to the normal direction according to the inserted stereographic triangle. The crystallographic variant analysis shown in Fig. 4 (a – c) indicates that six variants sharing the same parallel close-packed planes in the K-S

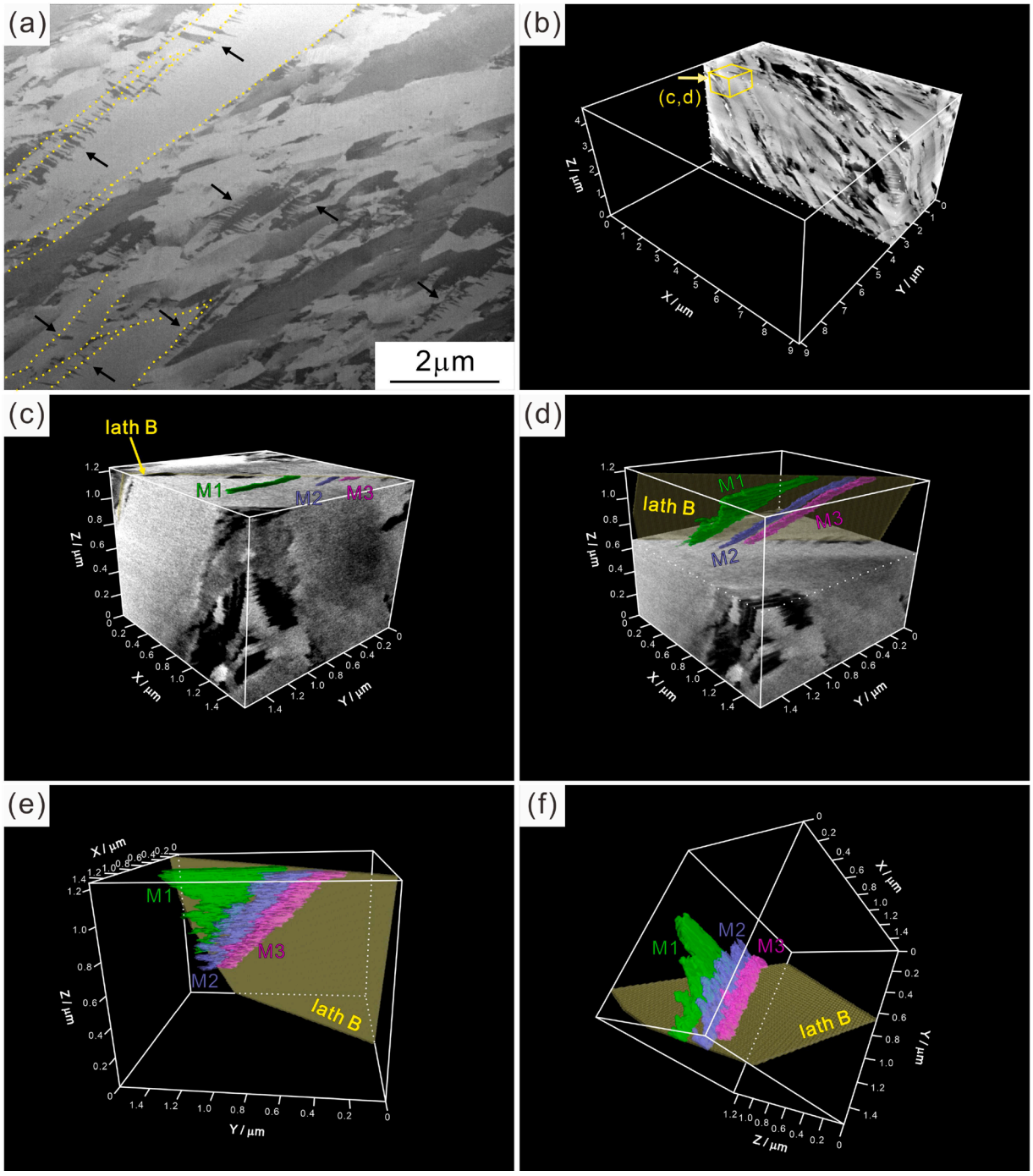


Fig. 5. (a) SEM image and (b-f) 3D reconstructed images via FIB-SEM serial sectioning. The volumes of twin-orientation-related intralath structures (M1 – M3) extracted through image analysis are shown in green, blue, and pink in (c – f). Some of the lath boundaries are indicated by dashed yellow lines in (a).

relationship ($(1\ 1\ 1)_A$ // $(0\ 1\ 1)_M$), namely V1 through V6, are formed in the region observed in (a); pink region: V1, light green region: V2, sky blue region: V3, red region: V4, muted green region: V5, and muted blue region: V6. There appears to be a tendency for V1/V4, V2/V5, and V3/V6 to form adjacent pairs. These pairings correspond to sub-block pairings frequently observed in low-carbon steels, which are characterized by small misorientations (theoretically 10.5 °) [4]. On the other hand, higher-magnification images in Fig. 4 (d – f) reveal that nanometer-scale domains of V1 are embedded inside the martensite plate of V2. Notably, the boundary between V1 and V2 is highly inclined relative to the lath boundary plane of V2. A similar configuration is observed in Fig. 4 (g-i), where small domains of V3 are present within the large martensite plate of V4, and their boundaries deviate significantly from the lath boundary plane of V4. It is also noteworthy that the observed specific combinations of variants (V1/V2, as well as V3/V4) exhibit a twin relationship (60 ° around $<1\ 1\ 1>_M$). Therefore, these small domains can be interpreted as "twin-orientation-related intralath structures".

According to the ACOM-TEM analysis (Fig. 4), the nanometer-scale intralath structures embedded within a given martensite plate, as indicated by black lines in the SEM image of Fig. 5(a), exhibit a twin relationship with the enclosing martensite plate. The 3D analysis results on the twin-orientation-related intralath structures are depicted in Fig. 5 (b – f). The volumes of three intralath structures were extracted through image analysis, and are shown in green, blue, and pink colors. The images in Fig. 5 (d – f) show the same volume viewed from different directions. We found that the twin-orientation-related intralath structures existing within a given martensite plate exhibit a plate-like morphology. Moreover, the boundary planes between these twin-orientation-related intralath structures and the enclosing martensite plate are nearly parallel, and all the twin-orientation-related intralath structures are connected to one side of the lath boundary. The crystallographic orientations of the boundary planes between the twin-orientation-related intralath structures and the enclosing martensite plates were determined for six pairs (two of V1/V2 pairs and four of V3/V4 pairs) using two-surface trace analysis based on the orientations obtained by ACOM-TEM, and the results are shown in Fig. 6((a): austenite coordinate system, (b): martensite coordinate system). For each intralath-enclosing lath boundary plane, two orientations are plotted in the martensite coordinate system: one based on each variant (for example, based on the orientations of V1 and V2). Different from the habit planes / lath boundary planes (Fig. 3 (c, d)), the orientations of intralath-enclosing lath boundary planes are distributed close to $\{1\ 1\ 1\}_A$ in the austenite coordinate system (Fig. 6(a)) and $\{0\ 1\ 1\}_M$ in the martensite coordinate system (Fig. 6(b)). While some of these planes correspond to the parallel close-packed planes in the K-S relationship of V1 - V6, others exhibit different orientations. It is worth emphasizing that these twin-orientation-related intralath structures are different from transformation twins introduced as a lattice-invariant deformation. As shown in the high-magnification STEM images of Fig. 7 (c, e), transformation twins are occasionally observed inside the martensite plates. These transformation twins are extremely fine, with an average thickness of approximately 5 nm. Compared with the intralath-enclosing lath boundaries depicted in Figs. 5 and 7(a), the boundary planes of the transformation twins are significantly sharper at the atomistic level (Fig. 7(e)). Moreover, the atomistic arrays are completely coherent across the transformation twin boundary. As reported by Casillas et al. [50], there are absolutely no additional phases at the twin boundary. Fig. 7 (b, d, f) show the selected area diffraction and fast Fourier transform patterns, together with the corresponding key diagrams, of the twin-orientation-related intralath structures (Fig. 7(b)) and the transformation twins (Fig. 7 (d, f)); the subscript "T" in the key diagrams denotes the indices corresponding to the intralath structures or transformation twins, and the cross markers indicate the double diffraction spots. The electron diffraction and fast Fourier transform patterns are consistent with both the intralath structures and the transformation twins, and from the orientation relationship with respect to the martensite matrix, it is difficult to distinguish between intralath structures and transformation twins. The transformation twins satisfy the edge-on condition in Fig. 7 (c, e), and the corresponding twin boundary planes are identified as $(1\ 1\ 2)_M$ based on the electron diffraction and fast Fourier transform patterns (Fig. 7 (d, f)). Therefore, we can consider that these transformation twins were introduced as a lattice-invariant deformation, similar to those observed in lenticular martensite and thin plate martensite [51–53]. On the other hand, the intralath – enclosing lath boundaries are not edge on in Fig. 7(a), and they are not parallel to $(1\ 1\ 2)_M$. As demonstrated in Fig. 6(b), those planes are parallel to $\{0\ 1\ 1\}_M$.

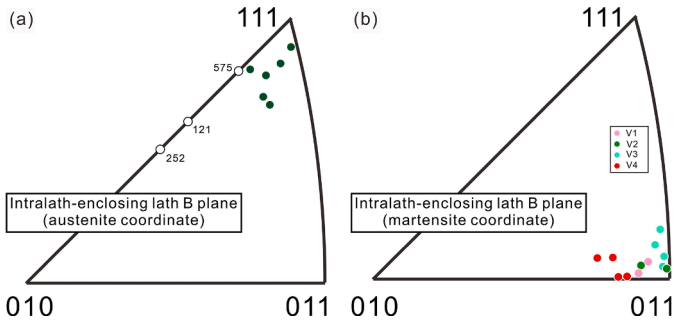


Fig. 6. Stereographic triangles showing the orientations of intralath-enclosing lath boundary planes (green circles) with respect to austenite coordinate system (a) and martensite coordinate system (b).

4. Discussion

4.1. Crystallographic features

As shown in Fig. 3 (c, d), the orientations of habit planes / lath boundary planes of martensite in the present 2Mn-0.5C steel are distributed between $(2\ 5\ 2)_A$ and $(2\ 9\ 5)_A$ in the austenite coordinate system, and around $(3\ 8\ 1)_M$ in the martensite coordinate system. In conjunction with previous studies [7], we identified a distinct carbon composition dependency on habit plane / lath boundary plane orientation, as the orientation progressively deviates from $(1\ 1\ 1)_A$ towards $(2\ 5\ 2)_A$ or $(2\ 9\ 5)_A$, and from $(0\ 1\ 1)_M$ towards $(3\ 8\ 1)_M$, with increasing carbon content. According to traditional understanding, the habit plane of martensite varies depending on its morphology; lath martensite: $(1\ 1\ 1)_A$ or $(5\ 7\ 5)_A$, butterfly martensite: $(2\ 5\ 2)_A$, lenticular martensite: $(2\ 9\ 5)_A$ or $(3\ 15\ 10)_A$, and thin plate martensite: $(2\ 9\ 5)_A$ or $(3\ 15\ 10)_A$ [54]. However, the present study demonstrates that this classification is not universally applicable. As shown in Figs. 2 and 3(c), the present 2Mn-0.5C steel exhibits a typical lath martensite structure, but its habit plane orientations range from $(2\ 5\ 2)_A$ to $(2\ 9\ 5)_A$. In the following, we discuss the origin of the habit plane orientation observed in the present study based on the PTMC.

The PTMC postulates that the habit plane corresponds to a macroscopically invariant plane, established through the combined effects of lattice deformation (specifically the Bain deformation for face-centered cubic (fcc) to body-centered cubic or tetragonal (bcc/bct) transformation), lattice-invariant deformation, and rigid-body rotation [31–34]. Within the double lattice-invariant deformation framework of PTMC [55–57], the overall shape deformation tensor ($\boldsymbol{F}$) is given by:

$$\boldsymbol{F} = \boldsymbol{R}\,\boldsymbol{B}\,\boldsymbol{P_1}\,\boldsymbol{P}_{>2} \quad (1)$$

Here, $\boldsymbol{B}$ represents the Bain deformation that converts the fcc lattice into bct; $\boldsymbol{P_1}$ and $\boldsymbol{P_2}$ correspond to lattice-invariant deformations that produce an undistorted plane; and $\boldsymbol{R}$ denotes the rigid-body rotation necessary to align the undistorted plane to an invariant plane. For the PTMC calculations, the lattice parameters were taken as a_A = 0.36313 nm for

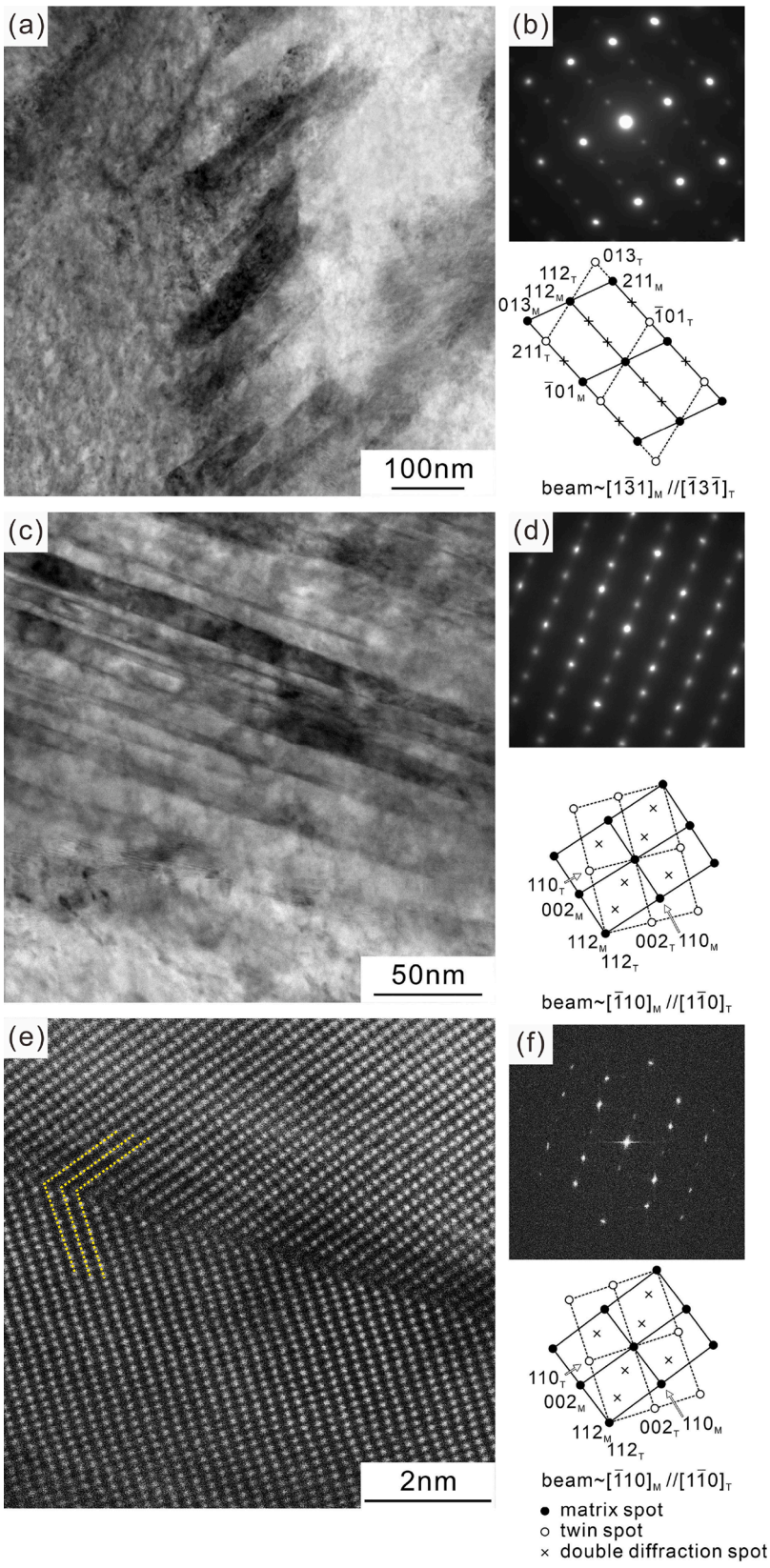


Fig. 7. (a, c, e) STEM images and (b, d, e) selected area diffraction / fast Fourier transform patterns and those key diagrams; (a, b) twin-orientation-related intralath structures and (c – f) transformation twins.

austenite and $a_M = 0.28974$ nm (with $c_M = a_M$) for martensite, based on ultra-low carbon steel data reported by Morito et al. [4]. To examine the effect of tetragonality, c_M value was virtually adjusted so that the c/a ratio became 1.02, 1.04, and 1.06. The lattice-invariant deformations of $\boldsymbol{P_1}$ and $\boldsymbol{P_2}$ are expressed as,

$$\boldsymbol{P_1} = \boldsymbol{I} + s_1\, \boldsymbol{d_1}\otimes\boldsymbol{p_1} \tag{2}$$

$$\boldsymbol{P_2} = \boldsymbol{I} + s_2\, \boldsymbol{d_2}\otimes\boldsymbol{p_2} \tag{3}$$

where s_1 and s_2 are shear magnitudes; $\boldsymbol{d_1}$ and $\boldsymbol{d_2}$ are shear directions; $\boldsymbol{p_1}$ and $\boldsymbol{p_2}$ are shear planes; $\boldsymbol{I}$ is the identity matrix. Based on the previous analyses of martensitic interphase boundaries [58], the $\boldsymbol{P_1}$ and $\boldsymbol{P_2}$ are set as $\boldsymbol{d_1} = [-1\ 0\ 1]_A$, $\boldsymbol{p_1} = (1\ 0\ 1)_A$, $\boldsymbol{d_2} = [0\ -1\ 1]_A$, $\boldsymbol{p_2} = (0\ 1\ 1)_A$. In the case of single lattice-invariant deformation, s_2 is set to zero. On the other hand, when double lattice-invariant deformations are considered, s_1 is increased from its value in the single lattice-invariant deformation case, and s_2 is then uniquely determined as the minimum value that satisfies the condition for forming an undistorted plane. The colored open symbols in Fig. 3(c) correspond to the results obtained from the double lattice-invariant deformation framework of the PTMC by increasing the value of s_1 in increments of 0.05 (starting from 0.250 for $c/a = 1$, from 0.255 for $c/a = 1.02$ and 1.04, and from 0.265 for $c/a = 1.06$). With increasing s_1, the value of s_2 required to satisfy the invariant-plane condition increases from 0 to 0.094 for $c/a = 1$, from 0 to 0.065 for $c/a = 1.02$, from 0 to 0.039 for $c/a = 1.04$, and from 0 to 0.011 for $c/a = 1.06$. We found that a larger magnitude of s_2 shifts the invariant plane approaching $(h\ l\ h)_A$ type orientation (for example, $(1\ 2\ 1)_A$ or $(2\ 5\ 2)_A$). In particular, high tetragonality ($c/a = 1.02 \sim 1.06$), combined with a large value of s_2, results in the invariant plane being close to $(2\ 5\ 2)_A$ plane. The observed habit plane orientations are distributed around the invariant plane orientations predicted for lattice-invariant deformation parameters of $s_1 = 0.260$, $s_2 = 0.025$, $c/a = 1.04$, and for $s_1 = 0.265$, $s_2 = 0.057$, $c/a = 1.02$.

Based on the empirical equation of the relationship between martensite tetragonality and carbon composition; $c/a = 1.00 + 0.045 \times$ mass % C [59], the c/a ratio of the martensite in the present 2Mn-0.5C steel is estimated to be 1.022, which is close to the value assumed in the PTMC calculations for the observed habit plane orientations. Here, the effect of Mn content on martensite tetragonality is not considered. We previously reported that shape deformation magnitude becomes minimum when the lattice invariant deformations are selected as invariant plane orientation close to $(h\ l\ h)_A$ type orientation [58]. Based on the above discussions, we can conclude that the habit plane orientations in the present 2Mn-0.5C martensitic steel are well explained by double lattice-invariant deformations associated with a high degree of tetragonality. However, the selected lattice-invariant deformation systems, particularly the magnitudes of the lattice-invariant deformations, do not correspond to those that minimize the overall shape deformation magnitude, suggesting a transient state toward its minimization. It should be noted that habit plane orientations in the IF steel deviate significantly from the invariant planes predicted by the PTMC. As proposed previously [7], this deviation could be attributed to dynamic changes in the lath boundary plane during growth, since the high Ms temperature promotes an increase in the fraction of low-energy, close-packed atomistic terraces (i.e., $(0\ 1\ 1)_M$ planes) to mitigate the net interfacial energy. Consequently, the habit plane orientations in the IF steel with high Ms temperature tend to approach the $(1\ 1\ 1)_A$ plane.

4.2. Local variant combination

The most significant finding in the present study is the clear identification of twin-orientation-related intralath structures (Figs. 4,5,6). These twin-orientation-related intralath structures are entirely distinct from transformation twins in terms of both morphology and crystallography. In particular, the intralath-enclosing lath boundary planes are close to $\{0\ 1\ 1\}_M$ (Fig. 6), whereas the boundaries of transformation twins are $(1\ 1\ 2)_M$ (Fig. 7). Oka and Okamoto [60] reported the presence of $\{1\ 0\ 1\}_M$-type twins with a thickness of less than several tens of nanometers, in addition to $\{1\ 1\ 2\}_M$ transformation twins, within lenticular martensite plates in 1.80C steel. They proposed that the exceptionally high tetragonality of martensite ($c/a = 1.078$) facilitates the formation of $\{1\ 0\ 1\}_M$-type twins to accommodate the shape strain or to inherit the shear strain associated with transformation twinning. Compared with the 1.80C steel studied by Oka and Okamoto [60], the tetragonality of martensite in the present 2Mn-0.5C steel is significantly lower ($c/a = 1.022$, estimated using the empirical equation [59]). Furthermore, the deviation of the intralath-enclosing lath boundary planes from the $\{0\ 1\ 1\}_M$ plane is substantial, ranging from 1.88 ° to 10.54 ° with an average of 5.21 ° (Fig. 6(b)). Therefore, we can conclude that the embedded nanometer-scale domains within the martensite plate are not $\{1\ 0\ 1\}_M$-type twins reported by Oka and Okamoto [60] but rather twin-orientation-related intralath structures.

It is unlikely that the twin-orientation-related intralath structures nucleate and grow inside a given martensite plate. Rather, as illustrated schematically in Fig. 8 (a-d), we consider that the orientation of martensite does not rotate into, nor evolve toward, a twin-related orientation; rather, a different martensite variant (the twin-related variant with respect to the original one) nucleates ahead of the longitudinal growth front of the original martensite plate. Subsequent lateral growth of the martensite plate then leads to the twin-orientation-related intralath structures being embedded within the martensite plate (Fig. 8 (e, f)). This is consistent with the observation results that all the twin-orientation-related intralath structures are connected to one side of the lath boundary (Fig. 5). Although it is extremely challenging to directly observe the growth behavior of martensite, it is reasonable to assume that the longitudinal growth rate of a martensite plate is much faster than its lateral growth rate. Indirect evidence for this is that lenticular martensite changes its substructure from twins to dislocations during lateral growth, likely due to local temperature rise inside the martensite plate, whereas no such substructure change was observed in the longitudinal direction [51,53].

In the following, we discuss the effect of martensite tetragonality on stress-induced variant selection based on micromechanics calculations, assuming that an enclosing martensite plate and intralath structure correspond to V1 and V2, respectively. Previous micromechanics calculations [7,61] indicated that the twin-related variant (V2) is preferentially formed due to its negatively large interaction energy with the stress field of austenite induced by the pre-existing martensite variant (V1), indicating stress-induced variant selection. According to the equivalent inclusion method proposed by Mura [62], the stress field (σ) in and around an inclusion (Ω) embedded in an infinitely extended matrix (D-Ω) is given by:

$$\Omega:\ \boldsymbol{\sigma}_{ij} = \boldsymbol{C}'_{ijkl}\left(\boldsymbol{S}_{klmn}\boldsymbol{\varepsilon}^{**}_{mn} - \boldsymbol{\varepsilon}^{*}_{kl}\right) = \boldsymbol{C}_{ijkl}\left(\boldsymbol{S}_{klmn}\boldsymbol{\varepsilon}^{**}_{mn} - \boldsymbol{\varepsilon}^{**}_{kl}\right) \tag{4}$$

$$D-\Omega:\ \boldsymbol{\sigma}_{ij} = \boldsymbol{C}_{ijkl}\boldsymbol{S}_{klmn}\boldsymbol{\varepsilon}^{**}_{mn} \tag{5}$$

$$\boldsymbol{\varepsilon}^{**} = \boldsymbol{\varepsilon}^{*} + \boldsymbol{\varepsilon}^{P} \tag{6}$$

where $\boldsymbol{C}'$ and $\boldsymbol{C}$ are elastic moduli of martensite and austenite, respectively; $\boldsymbol{S}$ is the Eshelby tensor; $\boldsymbol{\varepsilon}^*$ is the eigenstrain; and $\boldsymbol{\varepsilon}^{P}$ is the fictious equivalent eigenstrain. When both $\boldsymbol{C}'$ and $\boldsymbol{C}$ are known, $\boldsymbol{\varepsilon}^{**}$ can be evaluated from Eq. (4). The literature data of elastic moduli at high temperatures were used in the calculations: $C_{11} = 154$ GPa, $C_{12} = 122$ GPa, and $C_{44} = 77$ GPa for austenite at 1155 °C [63]; and $C_{11} = 170$ GPa, $C_{12} = 124$ GPa, and $C_{44} = 103$ GPa for ferrite (martensite) at 720 °C [64]. We assume that the martensite lath exhibits a thin-disk shape, with its broad face parallel to the invariant plane predicted by PTMC, and an aspect ratio of 0.2. The eigenstrain ($\boldsymbol{\varepsilon}^*$) associated with the formation of V1 is defined as:

$$\boldsymbol{\varepsilon}^{*} = \frac{1}{2}\left(\boldsymbol{F}^{T}\boldsymbol{F} - \boldsymbol{I}\right) \tag{7}$$

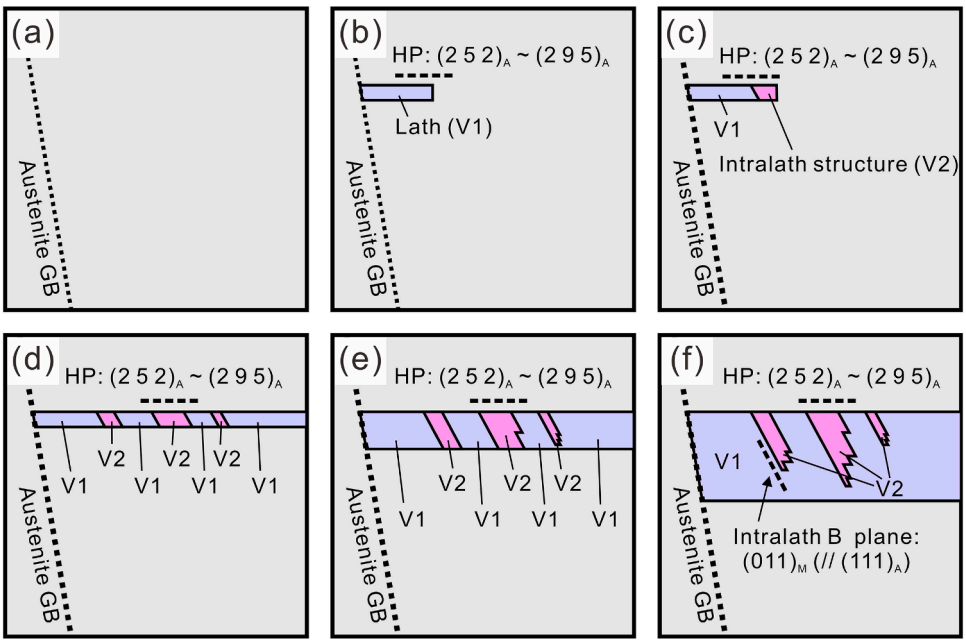


Fig. 8. Schematic illustration showing the formation sequence of twin-orientation-related intralath structures (V2) embedded within the martensite plate (V1).

where $\boldsymbol{F}$ is the shape strain tensor determined based on the PTMC (Eq. (1)). The volumetric interaction energy between the stress field generated by V1 in the surrounding austenite matrix (derived from Eq. (5)) and the transformation strain associated with another variant (Vn, $n = 1 \sim 24$) is given by:

$$E = -\frac{1}{2}\boldsymbol{\sigma}_{ij}\boldsymbol{\varepsilon}^{*}_{ij\ V_n} \tag{8}$$

A negative interaction energy indicates that the corresponding martensite variant is preferentially formed in the vicinity of the pre-existing V1. We assumed eigenstrains of another variant ($\boldsymbol{\varepsilon}^{*}_{ij\ Vn}$) to be the shear deformation caused by the first shear of the Bogers and Burgers model [65], represented by the slip system a/18 < 1 −1 −2> {1 −1 1}A, which corresponds to the primitive step of martensitic transformation. Fig. 9 summarizes the interaction energy between stress field generated by the formation of V1 and the eigenstrain of variants V1 to V6 (belonging to the same packet), as a function of martensite tetragonality. The shape deformation tensor of V1 at each tetragonality value was obtained by assuming the condition of minimum shape deformation magnitude, which corresponds to an invariant plane of (h l h)A type. We find that the order of interaction energies remains unchanged regardless of martensite tetragonality; V2 is the most preferentially formed under the stress field generated by V1, whereas V3 and V6 are not favored in terms of stress-induced variant selection. It is worth noting that the interaction energy of V2 significantly decreases with increasing martensite tetragonality, although a similar decreasing trend is also observed for V1, V4, and V5. This behavior may partly explain the reason why twin-related variants (V2) are more frequently observed in the present 2Mn-0.5C steel compared to our previous results for IF steel and 0.2C steel [7]. A comparable trend was quantitatively reported by Stormvinter et al. [16], who showed that the frequency of twin-related variant combination increases with increasing carbon content.

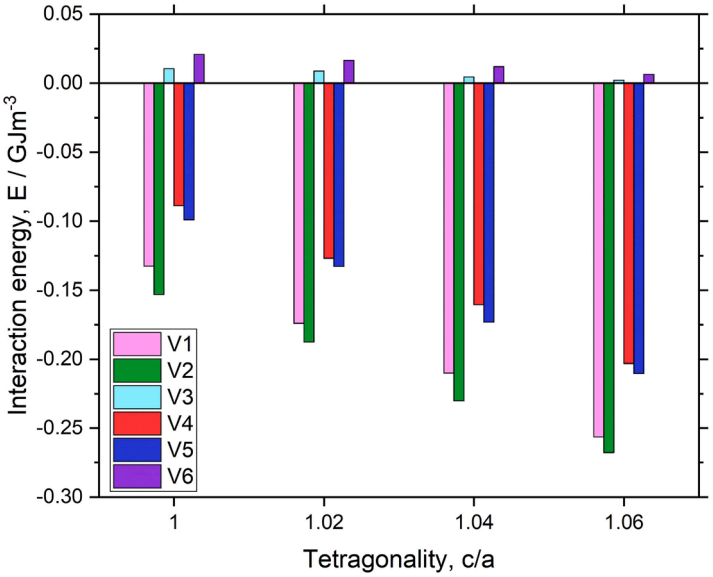


Fig. 9. Interaction energy between the stress field generated by V1 and the eigenstrains of variants V1 to V6 as a function of martensite tetragonality (c/a).

It has been reported that the microstructure of lath martensite, particularly the block and packet sizes, becomes finer with increasing carbon content [4]. The conventional interpretation of this phenomenon is that increasing carbon content, along with a simultaneous decrease in the Ms temperature, leads to hardening of the austenite matrix [66]. As a result, accommodation of transformation strain by plastic deformation becomes more difficult, and instead, self-accommodation through the formation of multiple variants is promoted. However, the aggregation of variants within a packet, namely V1 - V6, does not constitute an appropriate combination of variants for self-accommodation. In contrast, the combination of V1, V6, V16, and V17, which is frequently observed in lenticular martensite and thin plate martensite, is considered the most suitable for self-accommodation [17–21]. The micromechanics calculations shown in Fig. 9 indicate that increasing the martensite tetragonality facilitates the stress-induced formation of V1, V2, V4, and V5 around the pre-existing V1, with V2 being the most preferentially selected variant. This tendency is indeed observed in Figs. 4 and 5. The enhanced stress-induced variant selection may also contribute to the refinement of lath martensite structure with increasing carbon content.

To date, the strength and toughness of martensite have been primarily attributed to the block size, namely the size of a variant enclosed by high-angle boundaries [67–69]. However, twin-orientation-related intralath structures embedded within a martensite plate, which are identified in the present study (Figs. 4, 5, 6), may also play a critical role in determining mechanical performance. These intralath structures can act as barriers to dislocation motion and hinder cleavage crack propagation, thereby enhancing both the strength and toughness of the martensitic structure. Their influence is particularly important at the atomistic scale, where local stress concentration and deformation behavior are governed by the presence of such internal boundaries. Accordingly, we can propose that controlling the formation and spatial distribution of these twin-orientation-related intralath structures, potentially through optimized thermomechanical processing, emerges as a promising strategy for tailoring the mechanical properties of medium-carbon martensitic steels.

5. Conclusions

The present study investigated the microstructures of lath martensite, particularly local variant configuration and crystallographic features, in the medium-carbon steel via FIB-SEM serial sectioning and ACOM-TEM analyses. The key findings are summarized as follows:

1. Although the overall morphology of the lath structure appears complex and interwoven, each individual lath exhibits a relatively well-defined, plate-like shape, rather than a literal “lath”-like morphology. Two-surface trace analysis revealed that the orientations of habit planes (lath boundary planes) are distributed over a range from $(2\ 5\ 2)_A$ to $(2\ 9\ 5)_A$ in the austenite coordinate system, and are centered around $(3\ 8\ 1)_M$ in the martensite coordinate system. These observed habit plane orientations are well rationalized by the PTMC incorporating double lattice-invariant deformations and a high degree of martensite tetragonality.
2. The crystallographic variant analysis indicates that six variants sharing the same parallel close-packed planes in the K-S relationship, namely V1 through V6, are formed in a packet. There appears to be a tendency for V1/V4, V2/V5, and V3/V6 to form adjacent pairs. Moreover, we identified the existence of nanometer-scale domains exhibiting a twin relationship with the enclosing martensite plate, whose boundary planes are close to $\{0\ 1\ 1\}_M$. These domains can be interpreted as twin-orientation-related intralath structures, which are entirely distinct from $\{1\ 1\ 2\}_M$ transformation twins in terms of both morphology and crystallography. The clear identification of a twin-orientation-related intralath structure introduces a new hierarchical level, fundamentally challenging and redefining the conventional microstructural concept of lath martensite.
3. We consider that the twin-orientation-related intralath structure forms ahead of the longitudinal growth front of the original martensite plate. The subsequent lateral growth of the plate then leads to the twin-orientation-related intralath structures being embedded within the martensite plate. This interpretation is consistent with the observation results that all the twin-orientation-related intralath structures are connected to one side of the lath boundary.
4. Micromechanics calculations indicate that the formation of twin-orientation-related intralath structures (V2) is driven by stress-induced variant selection associated with the pre-formed martensite variant (V1). An increase in martensite tetragonality preferentially promotes the stress-induced formation of V2, while also facilitating the formation of V1, V4, and V5 around the pre-existing V1.

Data availability

The raw and processed data required to reproduce these findings cannot be shared at this time as the data also forms part of an ongoing study.

CRediT authorship contribution statement

Akinobu Shibata: Writing – original draft, Project administration, Methodology, Investigation, Funding acquisition, Formal analysis, Conceptualization. **Goro Miyamoto:** Writing – review & editing, Validation, Conceptualization. **Shigekazu Morito:** Writing – review & editing, Validation, Conceptualization. **Akiko Nakamura:** Visualization, Methodology, Investigation, Data curation. **Taku Moronaga:** Visualization, Methodology, Investigation, Data curation. **Houichi Kitano:** Visualization, Data curation. **Ivan Gutierrez-Urrutia:** Writing – review & editing, Validation. **Toru Hara:** Writing – review & editing, Validation.

Declaration of competing interest

The authors declare that they have no known competing financial interests or personal relationships that could have appeared to influence the work reported in this paper.

Acknowledgments

This study was financially supported by JSPS KAKENHI (Grant Numbers JP22K18910, JP23H01717 and JP23K26410) and MEXT Program: Data Creation and Utilization Type Material Research and Development Project Grant Number [JPMXP1122684766]. A part of this work was supported by ARIM of MEXT [JPMXP1223NM5284, JPMXP1224NM5108, and JPMXP1225NM5240], and by the Electron Microscopy Unit, National Institute for Materials Science (NIMS).

References

[1] G. Krauss, Martensite in steel: Strength and Structure, 273-275, Materials Science and Engineering A, 1999, pp. 40–57.
[2] A.R. Marder, G. Krauss, Formation of low carbon martensite in Fe-C alloys, Am. Soc. Met. Trans. Q. 62 (1969) 957–964.
[3] G. Krauss, A.R. Marder, The morphology of martensite in iron alloys, Metall. Trans. 2 (1971) 2343–2357.
[4] S. Morito, H. Tanaka, R. Konishi, T. Furuhara, T. Maki, The morphology and crystallography of lath martensite in Fe-C alloys, Acta Mater. 51 (2003) 1789–1799.
[5] S. Morito, X. Huang, T. Furuhara, T. Maki, N. Hansen, The morphology and crystallography of lath martensite in alloy steels, Acta Mater. 54 (2006) 5323–5331.

[6] C.C. Kinney, K.R. Pytlewski, A.G. Khachaturyan, J.W. Morris, The microstructure of lath martensite in quenched 9Ni steel, Acta Mater. 69 (2014) 372–385.
[7] A. Shibata, G. Miyamoto, S. Morito, A. Nakamura, T. Moronaga, H. Kitano, I. Gutierrez-Urrutia, T. Hara, K. Tsuzaki, Substructure and crystallography of lath martensite in as-quenched interstitial-free steel and low-carbon steel, Acta Mater. 246 (2023) 118675.
[8] L. Morsdorf, C.C. Tasan, D. Ponge, D. Raabe, 3D structural and atomic-scale analysis of lath martensite: effect of the transformation sequence, Acta Mater. 95 (2015) 366–377.
[9] T.T.T. Trang, D. Lee, Y.-U. Heo, Direct observation of the ledge-typed twin boundary in a martensitic steel, Acta Mater. 259 (2023) 119285.
[10] A.F. Gourgues, H.M. Flower, T.C. Lindley, Electron backscattering diffraction study of acicular ferrite, bainite, and martensite steel microstructures, Mater. Sci. Technol. 16 (2000) 26–40.
[11] M. Michiuchi, S. Nambu, Y. Ishimoto, J. Inoue, T. Koseki, Relationship between local deformation behavior and crystallographic features of as-quenched lath martensite during uniaxial tensile deformation, Acta Mater. 57 (2009) 5283–5291.
[12] S. Nambu, M. Michiuchi, Y. Ishimoto, K. Asakura, J. Inoue, T. Koseki, Transition in deformation behavior of martensitic steel during large deformation under uniaxial tensile loading, Scr. Mater. 60 (2009) 221–224.
[13] L. Morsdorf, O. Jeannin, D. Barbier, M. Mitsuhara, D. Raabe, C.C. Tasan, Multiple mechanisms of lath martensite plasticity, Acta Mater. 121 (2016) 202–214.
[14] A. Shibata, Y. Madi, J. Besson, A. Nakamura, T. Moronaga, K. Okada, I. Gutierrez-urrutia, T. Hara, Relationship between three-dimensional crack morphology and macroscopic mechanical properties of hydrogen-related fracture in martensitic steel, ISIJ Int. 64 (2024) 660–667.
[15] M. Nishida and K. Tsuzaki, Cp. 9 Martensitic Transformation, Physical Metallurgy 6th Ed., Elsevier, in press.
[16] A. Stormvinter, G. Miyamoto, T. Furuhara, P. Hedström, A. Borgenstam, Effect of carbon content on variant pairing of martensite in Fe–C alloys, Ascta Mater. 60 (2012) 7265–7274.
[17] J.C. Bokros, E.R. Parker, The mechanism of the martensite burst transformation in FeNi single crystals, Acta Metall. 11 (1963) 1291–1301.
[18] H. Okamoto, M. Oka, I. Tamura, Couplings of thin-plate martensites in an Fe-Ni-C alloy, Trans. Jpn. Inst. Met. 19 (1978) 674–684.
[19] A. Shibata, F. Ichikawa, H. Adachi, T. Yamasaki, N. Tsuji, Cooperative strain accommodation over grains in martensitic transformation from Fe-Ni nanocrystalline austenite, Philos. Mag. Lett. 97 (2017) 132–139.
[20] Y. Shinohara, S. Akabane, T. Inamura, Analysis of variant-pairing tendencies in lenticular martensite microstructures based on rank-1 connection, Sci. rep. 11 (2021) 14957.
[21] Y. Shinohara, M. Hishida, Y. Tanaka, T. Inamura, Analysis of thin-plate martensite microstructure in steel focusing on incompatibility and its visualization, Acta Mater. 259 (2023) 119275.
[22] S. Kumar, N.N. Pai, S. Manda, U. Tewary, D.T. Fullwood, S.K. Giri, S. Kundu, S.V.S. N. Murty, C.R. Anoop, I. Samajdar, Austenite residual stress and lath martensite variant selection in low carbon steels, Acta Mater. 289 (2025) 120885.
[23] J.R. Patel, M. Cohen, Criterion for the action of applied stress in the martensitic transformation, Acta Metall. 1 (1953) 531–538.
[24] M. Kato, T. Mori, Stress-induced martensite in single-crystals of an Fe-23Ni-5Cr alloy, Acta Metall. 24 (1976) 853–860.
[25] N.J. Wittridge, J.J. Jonas, J.H. Root, A dislocation-based model for variant selection during the γ-to-α′ transformation, Metall. Mater. Trans. A 32A (2001) 889–901.
[26] S. Kundu, H.K.D.H. Bhadeshia, Transformation texture in deformed stainless steel, Scr. Mater. 55 (2006) 779–781.
[27] S. Kundu, Prediction of transformation texture under complex rolling condition, Mater. Sci. Eng. A 516 (2009) 290–296.
[28] G. Miyamoto, N. Iwata, N. Takayama, T. Furuhara, Quantitative analysis of variant selection in ausformed lath martensite, Acta Mater. 60 (2012) 1139–1148.
[29] R. Ueji, A. Shibata, K. Ushioda, Y. Kimura, T. Ohmura, T. Inoue, Crystallographic orientation dependence of deformation-induced martensitic transformation of 1.3 GPa-class 0.6 %C bainitic steel with retained austenite, Scr. Mater. 194 (2021) 113666.
[30] A. Mirzaei, P.D. Hodgson, X. Ma, V.K. Peterson, E. Farabi, G.S. Rohrer, H. Beladi, The role of parent austenite grain size on the variant selection and intervariant boundary network in a lath martensitic steel, Mater. Sci. Eng. A 889 (2024) 145793.
[31] M.S. Wechsler, D.S. Lieberman, T.A. Read, On the theory of the formation of martensite, Trans. AIME 197 (1953) 1503–1515.
[32] J.S. Bowles, J.K. Mackenzie, The crystallography of martensite transformations I, Acta Metall. 2 (1954) 129–137.
[33] J.K. Mackenzie, J.S. Bowles, The crystallography of martensite transformations II, Acta Metall. 2 (1954) 138–147.
[34] M.S. Wechsler, On the theory of martensitic transformations. The generalized lattice invariant shear and the degeneracy of solutions for the cubic to tetragonal transformation, Acta Metall. 7 (1959) 793–802.
[35] B.P.J. Sandvik, C.M. Wayman, Characteristics of lath martensite: part I. Crystallographic and substructural features, Metall. Trans. 14A (1983) 809–822.
[36] B.P.J. Sandvik, C.M. Wayman, Characteristics of Lath Martensite: Part II. The martensite-Austenite Interface, Metallurgical Transaction A, 1983, pp. 823–834, 14 A.
[37] B.P.J. Sandvik, C.M. Wayman, Characteristics of Lath Martensite Part III. Some theoretical Considerations, Metallurgical Transaction A, 1983, pp. 835–844, 14 A.
[38] D.J. Rowenhorst, A. Gupta, C.R. Feng, G. Spanos, 3D Crystallographic and morphological analysis of coarse martensite: combining EBSD and serial sectioning, Scr. Mater. 55 (2006) 11–16.
[39] S. Morito, A. Hoang Pham, T. Ohba, T. Hayashi, T. Furuhara, G. Miyamoto, Three-dimensional observations of morphology of low-angle boundaries in ultra-low carbon lath martensite, Microscopy 66 (2017) 380–387.
[40] M. Mosayebi, P.-A. Deschênes, D. Paquet, L. Tôn-Thât, N. Bassim, Three-dimensional analysis of local and dominant habit planes in a lath martensitic stainless steel, Materialia 42 (2025) 102494.
[41] M. Mosayebi, D. Paquet, P.-A. Deschênes, L. Tôn-Thât, N. Bassim, Three-dimensional characterization of morphology and distribution of boundary networks in a low-carbon martensitic stainless steel, Mater. Charact. 229 (2025) 115456.
[42] M. Mosayebi, D. Paquet, P.-A. Deschênes, L. Tôn-Thât, B. Huang, N. Bassim, On the correlation between the habit plane and 3D morphology of lath martensite: a direct 3D observation using serial sectioning tomography of a low-carbon stainless steel, Scr. Mater. 255 (2025) 116367.
[43] H. Beladi, G.S. Rohrer, A.D. Rollett, V. Tari, P.D. Hodgson, The distribution of intervariant crystallographic planes in a lath martensite using five macroscopic parameters, Acta Mater. 63 (2014) 86–98.
[44] S. Kaar, K. Steineder, R. Schneider, D. Krizan, C. Sommitsch, New Ms-formula for exact microstructural prediction of modern 3rd generation AHSS chemistries, Scr. Mater. 200 (2021) 113923.
[45] T. Hara, K. Tsuchiya, K. Tsuzaki, X. Man, T. Asahata, A. Uemoto, Application of orthogonally arranged FIB–SEM for precise microstructure analysis of materials, J. Alloys Compd. 577 (2013) S717–S721.
[46] H. Kitano, T. Nagira, F. Yoshinaka, T. Sawaguchi, T. Yamashita, Y. Aoki, H. Fujii, Development of a method to evaluate strain in weld solidification using in-situ observations with high-brightness synchrotron X-rays, Sci. Technol. Adv. Mater.: Methods 4 (2024) 2403964.
[47] G. Miyamoto, N. Iwata, N. Takayama, T. Furuhara, Mapping the parent austenite orientation reconstructed from the orientation of martensite by EBSD and its application to ausformed martensite, Acta Mater. 58 (2010) 6393–6403.
[48] G. Miyamoto, N. Takayama, T. Furuhara, Accurate measurement of the orientation relationship of lath martensite and bainite by electron backscatter diffraction analysis, Scr. Mater. 60 (2009) 1113–1116.
[49] T. Furuhara, H. Kawata, S. Morito, G. Miyamoto, T. Maki, Variant selection in grain boundary nucleation of upper bainite, Metall. Mater. Trans. A 39A (2008) 1003–1013.
[50] G. Casillas, W. Song, A.A. Gazder, Twins or the omega phase: which is it in high carbon steels? Scr. Mater. 186 (2020) 293–297.
[51] R.L. Patterson, G.M. Wayman, The crystallography and growth of partially-twinned martensite plates in Fe-Ni alloys, Acta Metall. 14 (1966) 347–369.
[52] T. Maki, S. Shimooka, I. Tamura, Ms temperature and morphology of martensite in Fe-31 pct Ni-0.23 pct C alloy, Metall. Trans. 2 (1971) 2944–2945.
[53] A. Shibata, S. Morito, T. Furuhara, T. Maki, Substructures of lenticular martensites with different martensite start temperatures in ferrous alloys, Acta Mater. 57 (2009) 483–492.
[54] T. Maki, Microstructure and mechanical behaviour of ferrous martensite, Mater. Sci. Forum 56-58 (1990) 157–168.
[55] N.D.H. Ross, A.G. Crocker, A generalized theory of martensite crystallography and its application to transformations in steels, Acta Metall. 18 (1970) 405–418.
[56] D.P. Dunne, G.M. Wayman, An assessment of the double shear theory as applied to ferrous martensitic transformations, Acta Metall. 19 (1971) 425–438.
[57] P.M. Kelly, Crystallography of lath martensite in steels, Mater. Trans. JIM 33 (1992) 235–242.
[58] A. Shibata, T. Furuhara, T. Maki, Interphase boundary structure and accommodation mechanism of lenticular martensite in Fe–Ni alloys, Acta Mater. 58 (2010) 3477–3492.
[59] Z. Nishiyama, Martensitic Transformation, Academic Press, New York, 1978.
[60] M. Oka, H. Okamoto, Roles of (101)-alpha twinnings in martensitic-transformation of a 1.80 mass-percent carbon-steel, Mater. Trans. JIM 33 (1992) 229–234.
[61] A. Lambert-Perlade, A.F. Gourgues, A. Pineau, Austenite to bainite phase transformation in the heat-affected zone of a high strength low alloy steel, Acta Mater. 52 (2004) 2337–2348.
[62] T. Mura, Micromechanics, Kluwer Academic Publishers, Netherlands, 1987.
[63] J. Zarestky, C. Stassis, Lattice dynamics of γ-Fe, Phys. Rev. B 35 (1987) 4500–4502.
[64] D.J. Dever, Temperature dependence of the elastic constants in α-iron single crystals: relationship to spin order and diffusion anomalies, J. Appl. Phys. 43 (1972) 3293–3301.
[65] A.J. Bogers, W.G. Burgers, Partial dislocations on the {110} planes in the BCC lattice and the transition of the FCC into the BCC lattice, Acta Metall. 12 (1964) 255–261.
[66] T. Furuhara, T. Kaneshita, G. Miyamoto, Determining factors of grain size in bainite structure of Fe-2Mn-C alloys, Steel Res. Int. 95 (2024) 2400148.
[67] T. Ohmura, K. Tsuzaki, S. Matsuoka, Nanohardness measurement of high-purity Fe-C martensite, Scr. Mater. 45 (2001) 889–894.
[68] S. Morito, H. Yoshida, T. Maki, X. Huang, Effect of block size on the strength of lath martensite in low carbon steels, Mater. Sci. Eng. A 438-440 (2006) 237–240.
[69] A. Shibata, T. Nagoshi, M. Sone, S. Morito, Y. Higo, Evaluation of the block boundary and sub-block boundary strengths of ferrous lath martensite using a micro-bending test, Mater. Sci. Eng. A 527 (2010) 7538–7544.